Chapter

Control of Spin-Orbit Interaction in Conventional Semiconductor Quantum Wells

Jiyong Fu, Wei Wang and Minghua Zhang

Abstract

In this chapter, we demonstrate, focusing on GaAs quantum wells (QWs), a full control of spin-orbit (SO) interaction including both the Rashba and Dresselhaus terms in conventional semiconductor QWs. We determine the SO interaction in GaAs from single to double and triple wells, involving the electron occupation of either one or two subbands. Both the intraband and interband SO coefficients are computed. Two distinct regimes, depending on the QW width, for the control of SO terms, are found. Furthermore, we determine the persistent-spin-helix (PSH) symmetry points, where the Rashba and the renormalized (due to cubic corrections) Dresselhaus couplings are matched. These PSH symmetry points, at which quantum transport is diffusive (2D) for charge while ballistic (1D) for spin, are important for longtime and long-distance coherent spin control that is the keystone in spintronic devices.

Keywords: spintronics, spin-orbit interaction, Rashba term, Dresselhaus term, persistent spin helix, semiconductor, quantum well

1. Introduction

The spin-orbit (SO) interaction is a relativistic effect coupling spatial and spin degree of freedom via an effective magnetic field, facilitating spin manipulation in semiconductor nanostructures [1, 2]. For instance, the proposal of Datta and Das for a spin field-effect transistor highlights the use of the SO interaction of Rashba [3]. Recently, the SO effects [4] have attracted renewed interest in diverse fields of condensed matter, including the persistent spin helix (PSH) [5–8], topological insulators [9], and Majorana fermions [10, 11].

In zinc-blende-type crystals, such as GaAs, there are two dominant contributions to the SO interaction. The bulk inversion asymmetry leads to the Dresselhaus coupling [12], which in heterostructures contains both linear and cubic terms. The linear term mainly depends on the quantum-well confinement and the cubic one on the electron density [7, 13]. Additionally, the structural inversion asymmetry in heterostructures gives rise to the linear Rashba coupling [14], which can be electrically controlled by using an external bias [15, 16]. Extensive studies on the SO interaction have been focused on n-type GaAs/AlGaAs wells with only one-subband electron occupation [7, 13, 17]. Recently, quantum wells with two populated subbands have also drawn attention in both experiment [18–20] and theory [21–25],

because of emerging new physical phenomena including the intersubband coupling-induced spin mixing [19] and *crossed* spin helices [25].

In this chapter, we report our recent results on the electric control of SO interactions in conventional semiconductor quantum wells. *Firstly*, we focus on the case of single GaAs wells and performed a detailed self-consistent calculation to determine how the SO coupling (both the magnitude and sign) changes as a function of the gate voltage V_g. The gate-altered electron occupations between the first two subbands have been taken into account, and both the intraband and interband SO coefficients are computed. We find two distinct regimes for the electric control of SO interactions. *Secondly*, we consider the case of multiple wells and determine the SO interaction in GaAs from single to double and triple wells. Furthermore, we determine the persistent-spin-helix (PSH) symmetry points, where the Rashba and the renormalized (due to cubic corrections) Dresselhaus couplings are matched. These PSH symmetry points, at which quantum transport is diffusive (2D) for charge while ballistic (1D) for spin, are important for longtime and long-distance coherent spin control that is the keystone in spintronic devices.

2. Model Hamiltonian

The quantum wells that we consider are grown along the $z\|[001]$ direction. We start from the 8×8 Kane model, involving both conduction and valence bands, and use the folding down procedure [4, 24], to obtain an effective 3D Hamiltonian for electrons only [4, 13, 24]:

$$\mathcal{H}^{3\mathcal{D}} = \frac{\hbar^2 k_\parallel^2}{2m^*} - \frac{\hbar^2}{2m^*}\frac{\partial^2}{\partial z^2} + V_{sc}(z) + \mathcal{H}_{\mathcal{R}} + \mathcal{H}_{\mathcal{D}}, \tag{1}$$

where the first two terms refer to the kinetic contributions, in which m^* is the electron effective mass and $k_\parallel = \sqrt{k_x^2 + k_y^2}$ is the in-plane electron momentum with $x\|[100]$ and $y\|[010]$ directions. The third term V_{sc} describes the confining electron potential with the subscript *sc* indicating that it is determined self-consistently within the (Poisson-Schrödinger) Hartree approximation. The confining potential contains the structural potential V_w arising from the band offsets, the doping potential V_d, the electron Hartree potential V_e, and the external gate potential V_g [13, 23, 24]. The last two terms, $\mathcal{H}_{\mathcal{R}}$ and $\mathcal{H}_{\mathcal{D}}$, correspond to the Rashba and Dresselhaus SO interactions, respectively. Note that in Eq. (1), we have added the Dresselhaus term $\mathcal{H}_{\mathcal{D}}$ empirically [4, 13, 24], since to obtain $\mathcal{H}_{\mathcal{D}}$ one has to take into account the remote bands (e.g., **p**-conduction band) [4]. The Rashba term reads $\mathcal{H}_{\mathcal{R}} = \eta(z)\left(k_x\sigma_y - k_y\sigma_x\right)$ with $\eta(z) = \eta_w\partial_z V_w + \eta_H\partial_z\left(V_g + V_d + V_e\right)$ determining the Rashba strength and $\sigma_{x,y,z}$ the spin Pauli matrices. The constants η_w and η_H are determined by the bulk band parameters [13, 24]:

$$\eta_w = \frac{P^2}{3}\left(\frac{\delta_v/\delta_c}{E_g^2} - \frac{\delta_\Delta/\delta_c}{\left(E_g + \Delta\right)^2}\right), \tag{2}$$

$$\eta_H = -\frac{P^2}{3}\left(\frac{1}{E_g^2} - \frac{1}{\left(E_g + \Delta\right)^2}\right), \tag{3}$$

where E_g is the fundamental bandgap, P is the Kane parameter, and Δ is the split-off gap, in the well layer. The parameters δ_c, δ_v, and δ_Δ stand for band offsets

between well and barrier layers, of the conduction band, heavy hole (and light hole), and split-off hole, respectively. A schematic of the band offsets for a GaAs/AlGaAs well is shown in **Figure 1**. The Dresselhaus term is $\mathcal{H}_{\mathcal{D}} = \gamma\left[\sigma_x k_x\left(k_y^2 - k_z^2\right) + \text{c.c.}\right]$, with γ the bulk Dresselhaus parameter and $k_z = -i\partial_z$. From the 3D Hamiltonian (Eq. (1)), we are now ready to derive an effective 2D Hamiltonian for electrons. This 2D model is similar to the well-known Rashba model but now for wells with two subbands. We first self-consistently determine the spin-degenerate eigenvalues $\mathcal{E}_{\mathbf{k}_\parallel\nu} = \mathscr{E}_\nu + \hbar^2 k_\parallel^2/2m^*$ and the corresponding eigenspinors $|\mathbf{k}_\parallel\nu\sigma\rangle = |\mathbf{k}_\parallel\nu\rangle \otimes |\sigma\rangle$, $\langle \mathbf{r}|\mathbf{k}_\parallel\nu\rangle = \exp\left(i\mathbf{k}_\parallel \cdot \mathbf{r}_\parallel\right)\psi_\nu(z)$, of the well *in the absence* of SO interaction [24]. Here we have defined $\mathcal{E}_\nu$ (ψ_ν), $\nu = 1, 2$, as the ν_{th} quantized energy level (wave function) and $\sigma = \uparrow, \downarrow$ as the electron spin component along the z direction. We then can straightforwardly obtain an effective 2D model by projecting Eq. (1) onto the basis $\left\{|\mathbf{k}_\parallel\nu\sigma\rangle\right\}$. The effective 2D model with two subbands in the coordinate system $x_+\|(110)$, $x_-\|(1\bar{1}0)$ under the basis set $\left\{|\mathbf{k}_\parallel 1\uparrow\rangle, |\mathbf{k}_\parallel 1\downarrow\rangle, |\mathbf{k}_\parallel 2\uparrow\rangle, |\mathbf{k}_\parallel 2\downarrow\rangle\right\}$ reads [26]:

$$\mathcal{H}^{2D} = \left(\frac{\hbar^2 k_\parallel^2}{2m^*} + \mathcal{E}_+\right)\mathbf{1}\otimes\mathbf{1} - \mathcal{E}_-\tau_z \otimes \mathbf{1} + \mathcal{H}_{\mathcal{RD}}, \tag{4}$$

with $\mathcal{E}_\pm = (\mathcal{E}_2 \pm \mathcal{E}_1)/2$, $\mathbf{1}$ the 2×2 identity matrix (in both spin and orbital subspaces), and $\tau_{x_+,x_-,z}$ the Pauli ("pseudospin") matrices acting within the orbital subspace. The term $\mathcal{H}_{\mathcal{RD}}$ describes the Rashba and Dresselhaus SO contributions in terms of intra- and intersubband SO fields $\mathbf{B}_{SO}^{\nu}$ and $\mathbf{B}_{SO}^{12}$, respectively:

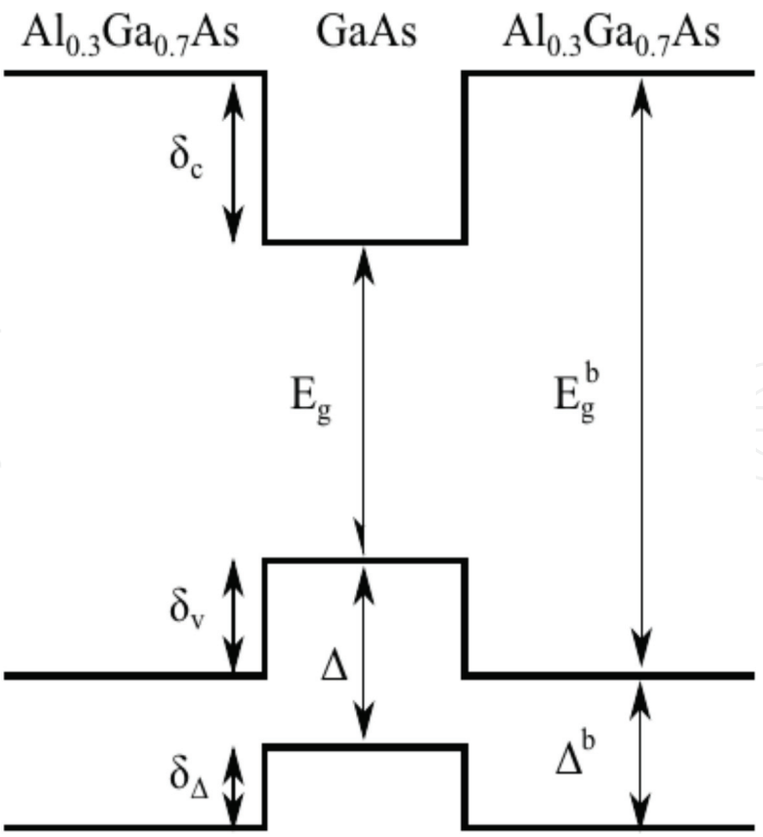

Figure 1.
A schematic of the band offsets for GaAs/AlGaAs well, in which E_g (E_g^b) and Δ (Δ^b) are the fundamental bandgap and the split-off gap in the well (barrier), respectively. δ_c, δ_v, and δ_Δ represent the band offsets between well and barrier layers, of the conduction band, heavy hole (and light hole), and split-off hole, respectively.

$$\mathcal{H}_{\mathcal{RD}} = \frac{1}{2} g\mu_B \sum_{\nu=1,2} \left[\tau_\nu \otimes \boldsymbol{\sigma} \cdot \mathrm{B}_{SO}^{\nu} + \tau_{x_+} \otimes \boldsymbol{\sigma} \cdot \mathbf{B}_{SO}^{12}\right], \tag{5}$$

with g the electron g factor, μ_B the Bohr magneton, and $\tau_{1,2} = (\mathbf{1} \pm \tau_z)/2$. Explicitly, the intrasubband SO field is

$$\mathrm{B}_{SO}^{\nu} = \frac{2}{g\mu_B} k \quad \left\{ \left[\left(\alpha_\nu - \beta_{\nu,\mathrm{eff}} \right) \sin\theta - \beta_{\nu,3} \sin 3\theta \right] \hat{\mathbf{x}}_+ - \right. \\ \left. \left[\left(\alpha_\nu + \beta_{\nu,\mathrm{eff}} \right) \cos\theta - \beta_{\nu,3} \cos 3\theta \right] \hat{\mathbf{x}}_- \right\}, \tag{6}$$

and the intersubband SO field is

$$\mathbf{B}_{SO}^{12} = \frac{2}{g\mu_B} k [(\eta - \Gamma) \cos\theta \hat{\mathbf{x}}_+ - (\eta + \Gamma) \sin\theta \hat{\mathbf{x}}_-], \tag{7}$$

where θ is the angle between $\mathbf{k}$ and the x_+ axis.

The Rashba and Dresselhaus SO coefficients, α_ν, β_ν, η, and Γ, appearing in Eqs. (6) and (7) read

$$\eta_{\nu\nu'} = \langle \psi_\nu | \eta_{\mathrm{w}} \partial_z V_{\mathrm{w}} + \eta_{\mathrm{H}} \partial_z \left(V_{\mathrm{g}} + V_{\mathrm{d}} + V_{\mathrm{e}} \right) | \psi_{\nu'} \rangle, \tag{8}$$

and

$$\Gamma_{\nu\nu'} = \gamma \langle \psi_\nu | k_z^2 | \psi_{\nu'} \rangle, \tag{9}$$

with the Rashba coefficients $\alpha_\nu \equiv \eta_{\nu\nu}$, $\eta \equiv \eta_{12}$ and the Dresselhaus coefficients $\beta_\nu \equiv \Gamma_{\nu\nu}$ and $\Gamma \equiv \Gamma_{12}$. The coefficient $\beta_{\nu,\mathrm{eff}} = \beta_\nu - \beta_{\nu,3}$ (Eq. (6)) is the renormalized "linear" Dresselhaus coupling, due to the cubic correction $\beta_{\nu,3} = \gamma k_\nu^2/4$, where $k_\nu = \sqrt{2\pi n_\nu}$ is the νth-subband Fermi wave number with n_ν the νth-subband occupation.

Note that the Rashba strength α_ν (Eq. (8)) can be written in terms of several distinct "individual" contributions, i.e., $\alpha_\nu = \alpha_\nu^{\mathrm{g}} + \alpha_\nu^{\mathrm{d}} + \alpha_\nu^{\mathrm{e}} + \alpha_\nu^{\mathrm{w}}$, with $\alpha_\nu^{\mathrm{g}} = \eta_{\mathrm{H}} \langle \psi_\nu | \partial_z V_{\mathrm{g}} | \psi_\nu \rangle$ the gate contribution, $\alpha_\nu^{\mathrm{d}} = \eta_{\mathrm{H}} \langle \psi_\nu | \partial_z V_{\mathrm{d}} | \psi_\nu \rangle$ the doping contribution, $\alpha_\nu^{\mathrm{e}} = \eta_{\mathrm{H}} \langle \psi_\nu | \partial_z V_{\mathrm{e}} | \psi_\nu \rangle$ the electron Hartree contribution, and $\alpha_\nu^{\mathrm{w}} = \eta_{\mathrm{w}} \langle \psi_\nu | \partial_z V_{\mathrm{w}} | \psi_\nu \rangle$ the structural contribution. Similar for the intersubband Rashba term $\eta = \eta^{\mathrm{g}} + \eta^{\mathrm{d}} + \eta^{\mathrm{e}} + \eta^{\mathrm{w}}$, the matrix element for each contribution is calculated between different subbands. For convenience, below we use $\alpha_\nu^{\mathrm{g}+d} = \alpha_\nu^{\mathrm{g}} + \alpha_\nu^{\mathrm{d}}$ and $\eta^{\mathrm{g}+d} = \eta^{\mathrm{g}} + \eta^{\mathrm{d}}$ for the contribution from the gate plus doping potential. We should emphasize that all of the SO coupling contributions above depend on the total self-consistent potential V_{sc} as our wave functions are calculated self-consistently.

It is worth noting that here we do not consider in our model the many-body effect-induced discontinuity of the electron density upon occupation of the second subband, as demonstrated by Goni et al. [27] and Rigamonti and Proetto [28] at zero temperature. As this discontinuity vanishes for T>30 K, we believe this is a minor effect in our system when $T = 75$ K. However, it is conceivable that related features can manifest in the SO couplings at zero temperature. Additional work is needed to investigate this interesting possibility.

3. Two distinct regimes for the control of SO interaction

In this section, we first introduce the structure of our wells and relevant parameters adopted in our simulation. Then we discuss our calculated SO couplings for the two distinct regimes. In either regime, we focus on a well having a two-subband electron occupation at zero bias (i.e., $V_g = 0$). By tuning V_g, we alter electron occupations from two subbands to one subband. For each value of V_g, within the self-consistent Hartree approximation, we determine the relevant SO strengths, i.e., the intrasubband α_ν, $\nu = 1, 2$, and intersubband η Rashba couplings, and similarly for the Dresselhaus term, the intrasubband β_ν and the intersubband Γ. Finally, the case of the two regimes in between is discussed as well.

3.1 System

The quantum wells we consider are similar to the samples experimentally studied by Koralek et al. [7]: the 001-grown GaAs wells of width w sandwiched between 48-nm $Al_{0.3}Ga_{0.7}As$ barriers. Our structure contains only one delta-doping (Si) layer, sitting 17 nm away from the well interface, with donor concentration n_d. Our prior simulated SO couplings [26] on these samples agree well with the data obtained via the transient-spin-grating technique [7], where there is no bias applied and all wells share the same areal electron density n_e. Here we go beyond the experiment in [7] by using an external bias, which can vary the electron density and control the SO interaction. At zero bias we assume $n_e = n_d$ [7].

The width w of quantum wells we consider ranges from 20 to 70 nm. Two distinct regimes of the SO interaction we found are marked off around $w = w_c = 30$–35 nm. Without loss of generality, we focus on a well of $w = 25$ nm for the first regime and a well of $w = 65$ nm for the second one. For the 25-nm well, we choose $n_d = 8.0 \times 10^{11}$ cm^{-2} and $T = 75$ K, the same as experimental parameters in [7], not only ensuring the electron occupation of the second subband at zero bias [26] but also retaining this second subband occupation over a broad range of V_g's. While for the 65-nm well, we choose relatively small values of n_d and T, i.e., $n_d = 4.0 \times 10^{11}$ cm^{-2} and $T = 0.3$ K, to exclude the electron occupation of a higher third subband.

3.2 Relevant parameters

In our GaAs/$Al_{0.3}Ga_{0.7}As$ wells, the values of relevant band parameters (see Eqs. (2) and (3)) are as follows: $E_g = 1.519$ eV and $\Delta = 0.341$ eV [4, 29, 30]. The corresponding counterparts of E_g and Δ in $Al_{0.3}Ga_{0.7}As$ barriers are $E_g^b = 1.951$ eV and $\Delta^b = 0.329$ eV [13, 24, 30]. As a consequence, we have the band offsets for conduction and valence bands, $\delta_c = \left(E_g^b - E_G\right) \times 60.4\% = 0.261$ eV, $\delta_v = E_g^b - E_G - \delta_c = 0.171$ eV, and $\delta_\Delta = \delta_v - \Delta + \Delta^b = 0.159$ eV [13, 24, 30]. For the Kane parameter, we choose $P = 1.0493$ nm [4, 29]. Then, we obtain $\eta_w = 3.97$°A2 and $\eta_H = -5.30$°A2 (Eqs. (2) and (3)). We treat the bulk Dresselhaus constant γ as an empirical parameter. We have recently done detailed calculations on a set of GaAs wells and have found via a realistic fitting procedure (theory and experiment) $\gamma \sim 11.0$ eV·A3 [13]. We use this value in our simulations, consistent with the one obtained in a recent study by Walser et al. [31].

3.3 Numerical outcome: two distinct regimes

Below we discuss our self-consistent outcome for the SO couplings. We present our calculated intra- and intersubband SO couplings in the two distinct regimes. The behavior of the SO interaction in the first regime as a function of the gate voltage is usual. As a consequence, we mainly focus on the second regime, in which new features of the SO interaction emerge.

3.3.1 Intrasubband SO couplings: both Rashba and Dresselhaus terms

We consider in the first regime a well of $w = 25$ nm. In **Figure 2(b)**, we show the dependence of Rashba α_ν ($\nu = 1, 2$) and Dresselhaus β_ν coefficients of the two subbands on V_g. We find that α_1 and α_2 have the same sign and they both decrease to zero near the symmetric configuration (at $V_g \sim 0.36$ eV) (see arrow in **Figure 2(b)**) and further change their sign. For the confining electron potential V_{sc} and wave functions ψ_ν in this symmetric geometry of the well, see **Figure 2(a)**. Clearly, our wells are asymmetric at $V_g = 0$ because of the one-side delta doping. In contrast to the Rashba term, we find that the Dresselhaus couplings $\beta_\nu = \gamma\langle\psi_\nu|k_z^2|\psi_\nu\rangle$ remain essentially constant with V_g. The inset in **Figure 2(b)** shows the electron density n_ν of the two subbands with $n_1 + n_2 = n_e$ as a function of V_g, and the second subband starts to be unpopulated around $V_g \sim 0.5$ eV.

Now, we turn to the second regime, in which we consider a well of $w = 65$ nm, as shown in **Figure 2(c)**. As opposed to the first regime, we find that α_1 and α_2 could have opposite signs. This is because electrons occupying the first and second subbands tend to be distributed on opposite sides for a wide well, as a result of the

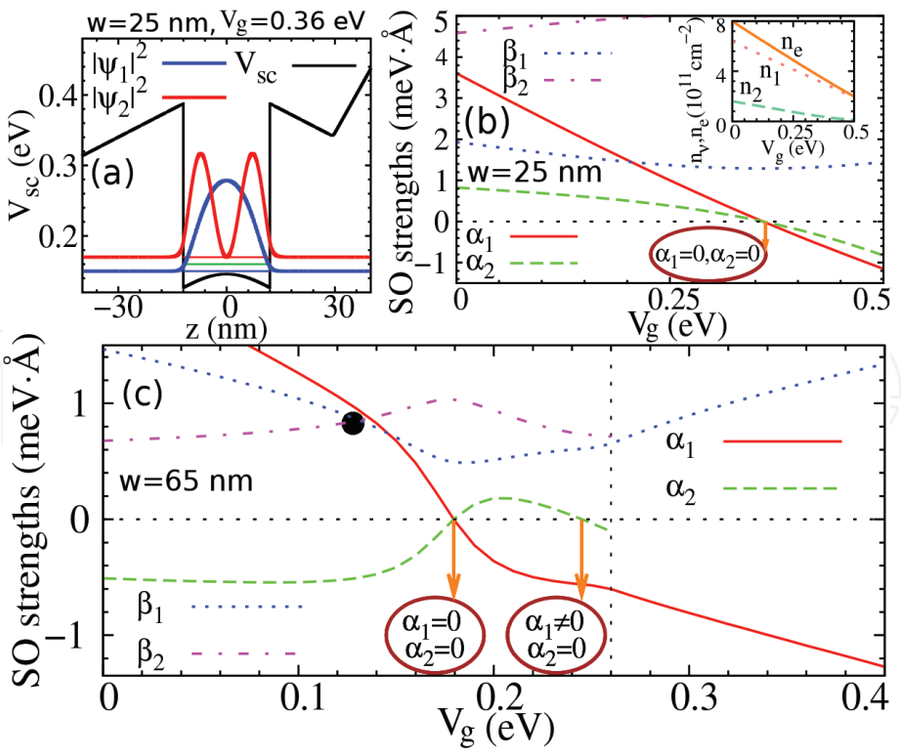

Figure 2.
(a) Self-consistent potential V_{sc} and wave function profiles ψ_ν of a 25-nm well at $V_g = 0.36$ eV (symmetric configuration). The horizontal lines inside the well respectively indicate the two-subband energy levels and the Fermi level. Gate control of Rashba α_ν and Dresselhaus β_ν SO couplings, for the 25-nm (b) and 65-nm wells (c). In (b), the inset shows electron density n_ν with $n_1 + n_2 = n_e$ as a function of V_g. In (c), the vertical dashed line at $V_g \sim 0.26$ eV marks regions of one- and two-band occupations. The temperature is chosen at 75 K for the 25-nm well and 0.3 K for the 65-nm well, from Wang et al. [32].

electron Hartree potential created "central barrier"; see **Figure 3**(**a**)–(**c**). We emphasize that the sign of SO couplings is crucial in diverse subjects of the field of spintronics, e.g., the persistent skyrmion lattice [25], the nonballistic spin field transistor operating with orthogonal spin quantization axes [33], and the transition from a topological insulator to Dirac semimetal [34].

To see more details about the sign change of Rashba couplings, we show in **Figure 3**(**d**) and (**e**) the gate dependence of distinct contributions of α_1 and α_2 separately, i.e., α_ν^{e}, α_ν^{w}, and $\alpha_\nu^{\mathrm{g+d}}$. For the structural contribution,

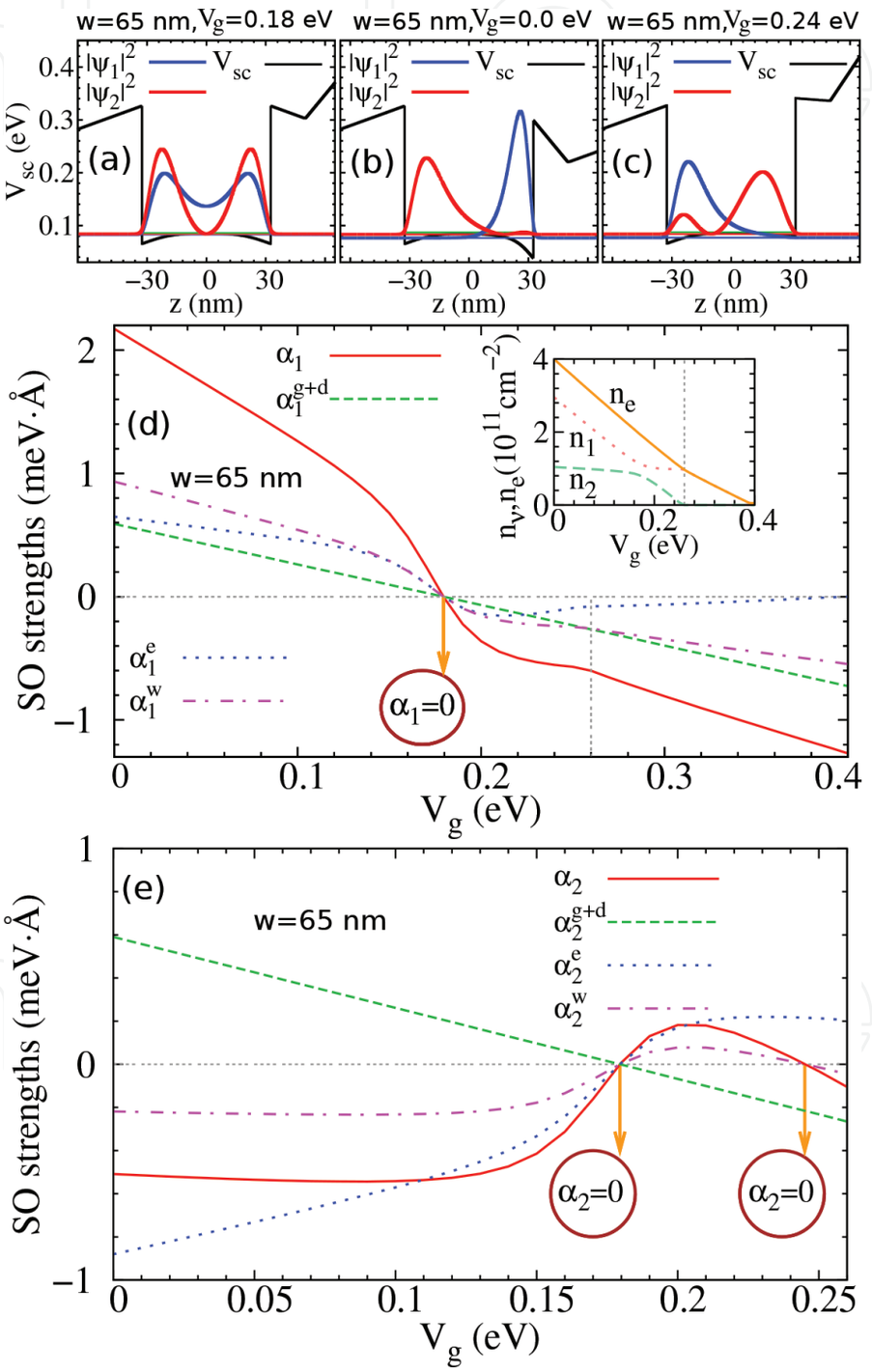

Figure 3.
(a)–(c) Potential V_{sc} and wave function profiles ψ_ν ($\nu = 1, 2$) for a 65-nm well at three values of voltages, with $V_g = 0.18$ (a), 0 (b), and 0.24 eV (c). The horizontal lines inside the well indicate the two-subband energy levels and the Fermi level. Dependence of different contributions to the intrasubband Rashba strength of the first (d) and second (e) subbands on the gate voltage for the 65-nm well. In (d), the inset shows the electron density n_ν with $n_1 + n_2 = n_e$ as a function of gate voltage. The vertical dashed line in (d) (and inset) marks regions of one- and two-band occupations. The temperature is chosen at 0.3 K, from Wang et al. [32].

$\alpha_\nu^{\mathrm{w}} \propto \langle \psi_\nu | \partial_z V_{\mathrm{w}} | \psi_\nu \rangle = |\psi_\nu(w/2)|^2 - |\psi_\nu(-w/2)|^2$ [26], α_1^{w} is dominated by the first term, while α_2^{w} is dominated by the second term, due to the already discussed tendency of the subband wave functions of ψ_1 and ψ_2 to respectively localize on the right and left halves of the well (zero bias for instance). This leads to opposite signs between α_1^{w} and α_2^{w}. Similarly, for $\alpha_\nu^{\mathrm{e}} \propto \langle \psi_\nu | \partial_z V_{\mathrm{e}} | \psi_\nu \rangle$, the electron Hartree contributions of the two subbands have opposite signs as well since V_{e} mostly has opposite slopes with respect to z for $z>0$ and $z<0$ [24]. However, for $\alpha_\nu^{g+d} \propto \langle \psi_\nu | \partial_z (V_{\mathrm{g}} + V_{\mathrm{d}}) | \psi_\nu \rangle$, the corresponding contributions of the two subbands have the same sign, due to the fact that the gate plus doping potential is linear across the well region. The relative sign of the total contribution to α_1 and α_2 depends on the interplay of the three constituents as a function of gate voltages.

From **Figure 3(e)**, we also find that α_2 remains essentially constant with V_{g} at lower voltages, precisely, as its constituent α_2^{w} behaves except for a prefactor difference. In contrast, it is found that α_1 sensitively depends on V_{g} in the whole parameter range studied here. Moreover, α_1 and α_2 become zero (see arrow in **Figure 3(d)** and left arrow in **Figure 3(e)**) across the symmetric configuration, corresponding to $V_{\mathrm{g}} \sim 0.18$ eV. Interestingly, we observe that α_2 can even attach zero at $V_{\mathrm{g}} \sim 0.24$ eV (see right arrow in **Figure 3(e)**), at which the well is very asymmetric (**Figure 3(c)**).

Before moving into the Dresselhaus couplings in this second regime, it is worth noting that the electron densities of the two subbands exhibit the anticrossing-like behavior near the symmetric configuration (at $V_{\mathrm{g}} \sim 0.18$ eV), as shown in the inset of **Figure 3(d)**. The feature of anticrossing of electron densities has been experimentally observed in double wells by Fletcher et al. [35], thus implying that our wells in the second regime do behave like *effective* double wells.

In **Figure 2(c)**, we show the linear Dresselhaus couplings $\beta_\nu = \gamma \langle \psi_\nu | k_z^2 | \psi_\nu \rangle$ in the second regime. We observe that the inequality $\beta_1 < \beta_2$, which is valid in the first regime, only holds in configurations near the symmetric geometry. However, if the well is very asymmetric, i.e., at $V_{\mathrm{g}} = 0$, we find $\beta_1 > \beta_2$ [see crossing (black dot) between β_1 and β_2 in **Figure 2(c)**], in contrast to the first regime.

Now, we are ready to determine the persistent-spin-helix (PSH) symmetry points of the two subbands, at which the Rashba α_ν and the renormalized linear Dresselhaus $\beta_{\nu,\,eff}$ (due to cubic corrections) are equal in strength, i.e., $\alpha_\nu \approx \beta_{\nu,\,eff}$, as shown in **Figure 4**. We observe that $\alpha_1 \approx \beta_{1,\,eff}$ takes place at $V_{\mathrm{g}} \sim 0.17$ eV (see right arrow in **Figure 4**) for the first subband, while $\alpha_2 \approx -\beta_{2,\,eff}$ always holds over the range of $V_{\mathrm{g}} = 0 - 100$ meV (see left arrow in **Figure 4**) for the second subband. This is possibly facilitating the locking of the PSH symmetry in practice. Note that in contrast to the well matched $|\alpha_2|$ and $\beta_{2,\,eff}$ here, a deviation between them can possibly occur for other wells with strong SO couplings (e.g., InAs-based wells). However, this deviation can always be possibly overcome by properly varying the electron density, which controls the cubic $\beta_{2,3}$—thus tuning $\beta_{2,\,eff}$ to match with $|\alpha_2|$. These symmetry points are also crucial for the persistent skyrmion lattice [25] as well as the nonballistic spin field effect transistors [5] operating with orthogonal spin quantization axes [33].

We emphasize that, for the PSH symmetry points that we determined above, the effect of the interband SO couplings (see Section 3.3.2) and of the random Rashba coupling [36–39] has been ignored. For the former, it is only relevant near the crossing(s) of the two-subband branches, as discussed in [25]. For the latter, it may in general destroy the helix but has a negligible effect on the results for our wells here [26].

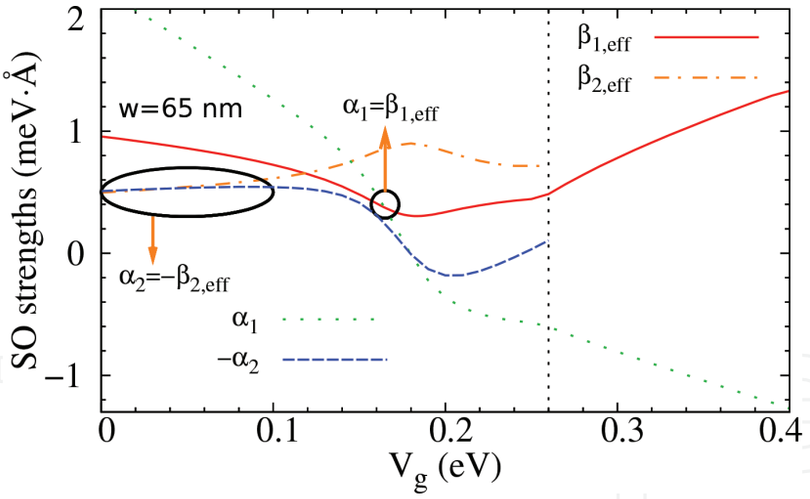

Figure 4.
The dependence of intrasubband Rashba α_ν and renormalized Dresselhaus $\beta_{\nu,eff}$ coefficients on V_g for the 65-nm well. The vertical dashed line marks regions of one- and two-band occupations. The temperature is held fixed at 0.3 K, from Wang et al. [32].

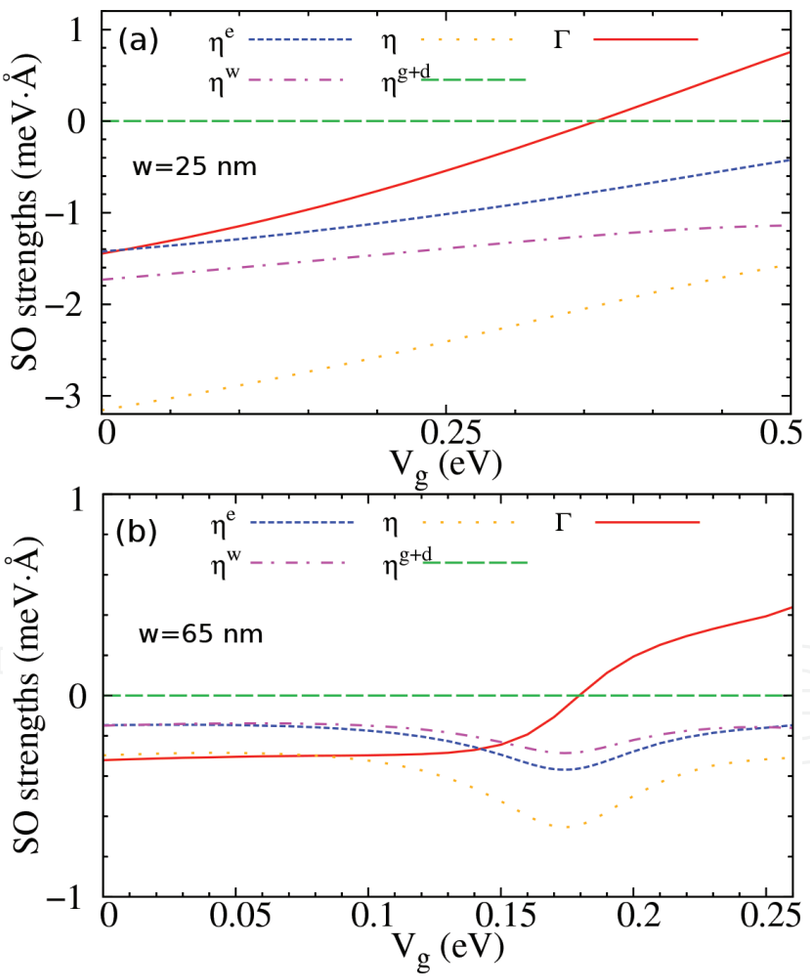

Figure 5.
Gate control of intersubband Rashba η and Dresselhaus Γ strengths for a 25-nm well (a) and a 65-nm well (b) the temperature is chosen at 75 K for the 25-nm well and 0.3 K for the 65-nm well, from Wang et al. [32].

3.3.2 Intersubband SO couplings: both Rashba and Dresselhaus terms

Below we turn to the interband SO terms. Referring to the first regime, in **Figure 5**(**a**), we show the intersubband Rashba coupling η and its distinct

constituents including η^{g+d}, η^{e}, and η^{w} and Dresselhaus coupling Γ for a well of $w = 25$ nm. We find that both η and Γ exhibit basically the linear behavior with V_g. Owing to the orthogonality between ψ_1 and ψ_2, the gate plus doing contribution η^{g+d} vanishes. As for the constituents η^{w} and η^{e}, the dominant variation with the gate is the latter as the electron density in wells changes with V_g, even though the magnitude of η^{w} is greater than η^{e}.

For the second regime, we show in **Figure 5**(**b**) the intersubband SO couplings for a well of $w = 65$ nm. In contrast to the first regime, here η largely remains constant as V_g increases. And a maximum of $|\eta|$ occurs at $V_g \sim 0.18$ eV (symmetric configuration). This arises from the fact that the wave functions of the two subbands, ψ_1 and ψ_2, are mostly separated in very asymmetric configurations (**Figure 3**(**b**) and (**c**)), which renders η (depending on the overlap of ψ_1 and ψ_2) almost constant and relatively weak. Similar to η, Γ also weakly depends on the gate except for configurations of the well near the symmetric geometry. Finally, we emphasize that, for wide and asymmetric *enough* wells, where ψ_1 and ψ_2 have vanishing overlap, both η and Γ tend to be zero.

3.4 Two regimes in between for the control of SO couplings

Now, it is clear that the SO couplings show distinct behaviors for the two regimes. By analyzing SO couplings for a set of wells of $w = 20 - 70$ nm, below we

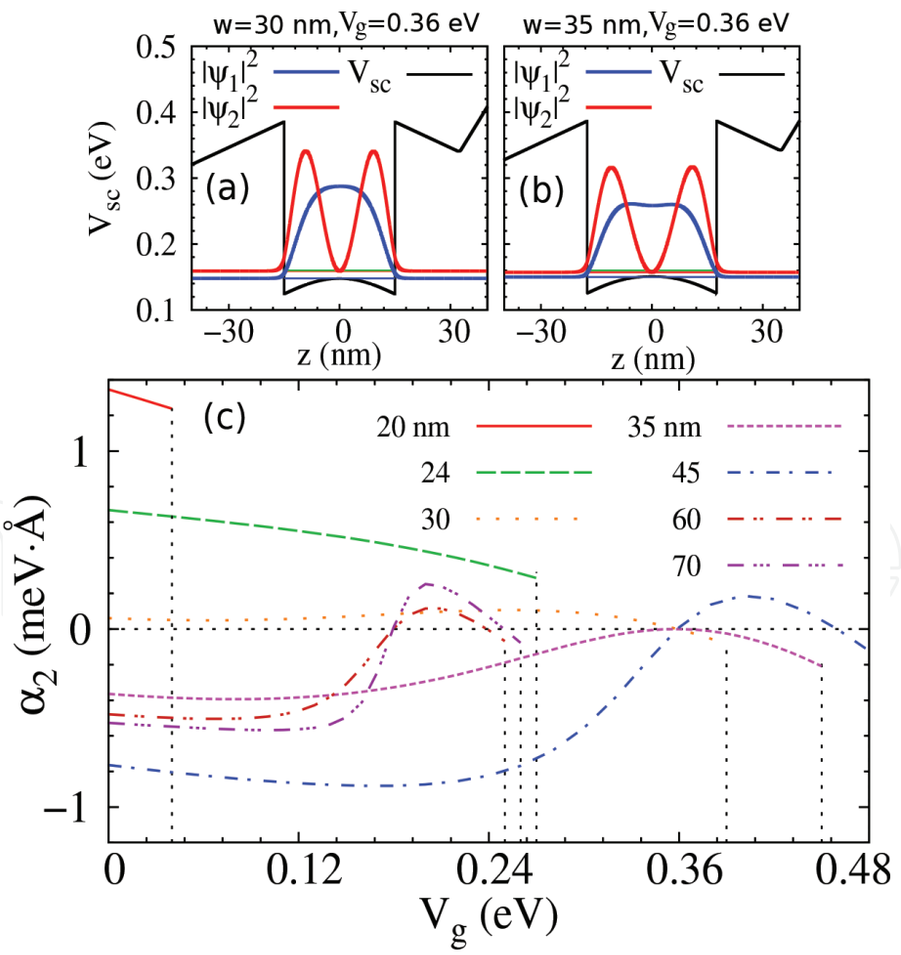

Figure 6.
Confining potential V_{sc} and wave function profiles ψ_ν in GaAs wells at $V_g \sim 0.36$ eV (symmetric geometry), for a 30-nm well (a) and a 35-nm well (b). the horizontal lines inside the wells indicate the two-subband energy levels and the Fermi level (c). the dependence of intrasubband Rashba α_2 of the second subband on V_g, for a set of wells of w = 20,24,30,35,45,60, and 70 nm. The vertical dashed lines mark regions of one- and two-band occupations. The temperature is held fixed at 0.3 K, from Wang et al. [32].

discuss how the two regimes transit from one to the other. To explore this, we only focus on α_2, which is mostly in contrast between the two regimes.

In **Figure 6**(**c**), we show the dependence of α_2 on V_g. Clearly, for the 20- and 24-nm wells, α_2 changes almost linearly, showing the usual behavior of the Rashba coupling, as demonstrated in the first regime. However, for the wells of $w = 45$, 60, and 70 nm, we observe the unusual behavior, which is referred to the second regime. When w in the range of $w = 30 - 35$ nm, the gate dependence of α_2 behaves in between the two regimes, i.e., there is neither the linear behavior in the first regime nor the sign of double changes in the second one. To gain more insight into this, we examine the confining potential V_{sc} and wave function profiles ψ_ν for the wells of $w = 30$ and 35 nm (**Figure 6**(**a**) and (**b**)), which are used to determine the SO coupling. It is clear that the envelope wave functions for the 30- and 35-nm wells look like a bridge connecting the two regimes, cf. **Figure 2**(**a**) for the first regime, **Figure 3**(**a**) for the second regime, and **Figure 6**(**a**) and (**b**) for the two regimes in between.

To deplete the second subband occupation, it is clear that a wider well requires in general a larger value of gate voltage (see vertical dashed lines for wells of $w = 20 - 45$ nm), as the confinement becomes weaker for a wider well. However, for the 60- and 70-nm wells (see vertical dashed lines for wells of $w = 60 - 70$ nm), we find that the voltages needed to deplete the second subband occupation are even less than the one for the 24-nm well. This is attributed to the low electron density we choose for wide wells, the choice of which is to exclude the electron occupation of a higher third subband.

4. Control of SO interaction from single to double and triple wells

With the knowledge of the SO interaction in single wells (Section 3), below we consider the case of multiple wells and determine the electrical control of the SO interaction in GaAs from single to double and triple wells.

4.1 System

The main structure of our well is again similar to the samples experimentally studied by Koralek et al. [7]: the 001-grown GaAs well of width $w = 26$ nm sandwiched between 48-nm $Al_{0.3}Ga_{0.7}As$ barriers. To have double (triple) wells, we introduce one (two) additional $Al_xGa_{1-x}As$ barrier layers of length $b = 3$ nm embedded inside the above structure. We choose the total electron density $n_e = 6.0 \times 10^{11}$ cm^{-2}. The temperature is held fixed at $T = 0.3$ K. Note that we choose relatively low n_e and T, instead of the experimental values $n_e = 8.0 \times 10^{11}$ cm^{-2} and $T = 75$ K in [7], on the one hand, to ensure the second subband electron occupation and on the other hand, to exclude the electron occupation of a higher third subband, for all values of V_gs studied here.

4.2 SO coupling coefficients

To explore the SO features from single to double and triple wells, firstly, we focus on the case of having only one $Al_xGa_{1-x}As$ additional barrier embedded at the center of the system.

In **Figure 7**(**a**) and (**b**), we show the gate dependence of intrasubband Rashba terms in our GaAs/$Al_{0.3}Ga_{0.7}As$ wells, for several Al contents x of the central barrier $Al_xGa_{1-x}As$. At $x = 0$ (single well), we find the usual scenario, i.e., α_1 and α_2 have

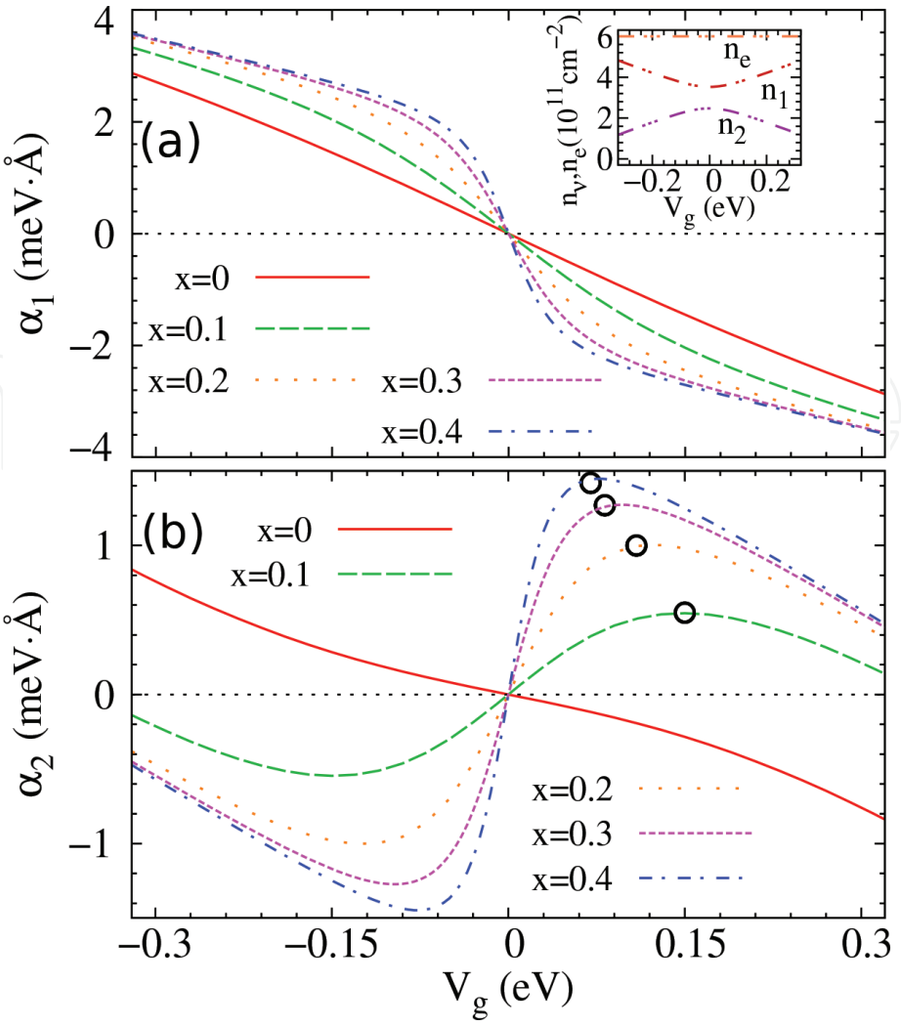

Figure 7.
Intrasubband Rashba α_1 (a) and α_2 (b) couplings as a function of V_g in GaAs/$Al_{0.3}Ga_{0.7}As$ wells for several Al contents x of a central barrier $Al_xGa_{1-x}As$. In (a), the inset shows the gate dependence of electron occupations n_1, n_2, and $n_e = n_1 + n_2$. In (b), the black circles indicate where α_2 exhibits the maximum, from Wang et al. [40].

the same sign and both change almost linearly with V_g. In this case, electrons occupying the first and second subbands spread over the whole well region (**Figure 8**(**a**)) and "see" the same fields (i.e., slope of potentials) that determine Rashba couplings (Eq. (8)). Thus, the above behavior of α_ν with V_g follows. In contrast, when x is away from zero (double well), electrons of the two subbands tend to localize on the left and right sides of the well, respectively, due to the effect of the central barrier (**Figure 8**(**b**) and (**c**)). This results in the opposite signs of α_1 and α_2, as the local field on the left and right sides of the well is almost reversed; see potential profiles in wells shown in **Figure 8**(**b**) and (**c**). In addition, α_2 first increases with V_g, while peaks at some point depending on x and further decreases, following from the compensated interplay of *local* fields (i.e., electron Hartree plus structural well) and the *universal* external gate field. For a larger value of x, α_2 increases with V_g more abruptly before it peaks, see black circles in **Figure 7**(**b**) for a set of values of x. Note that α_1 in magnitude consistently increases with V_g, since the local fields and the universal external gate field contribute to α_1 constructively.

Figure 8(**c**) shows the dependence of linear intrasubband Dresselhaus coupling $\beta_\nu = \gamma\langle k_z^2 \rangle$ on V_g. As opposed to α_ν, we find that β_ν is weakly dependent on V_g ($\pm \sim 0.5$ meV Å) for all values of x considered here. On the other hand, as x increases, the coupling between the left and right sides of the well is getting weaker,

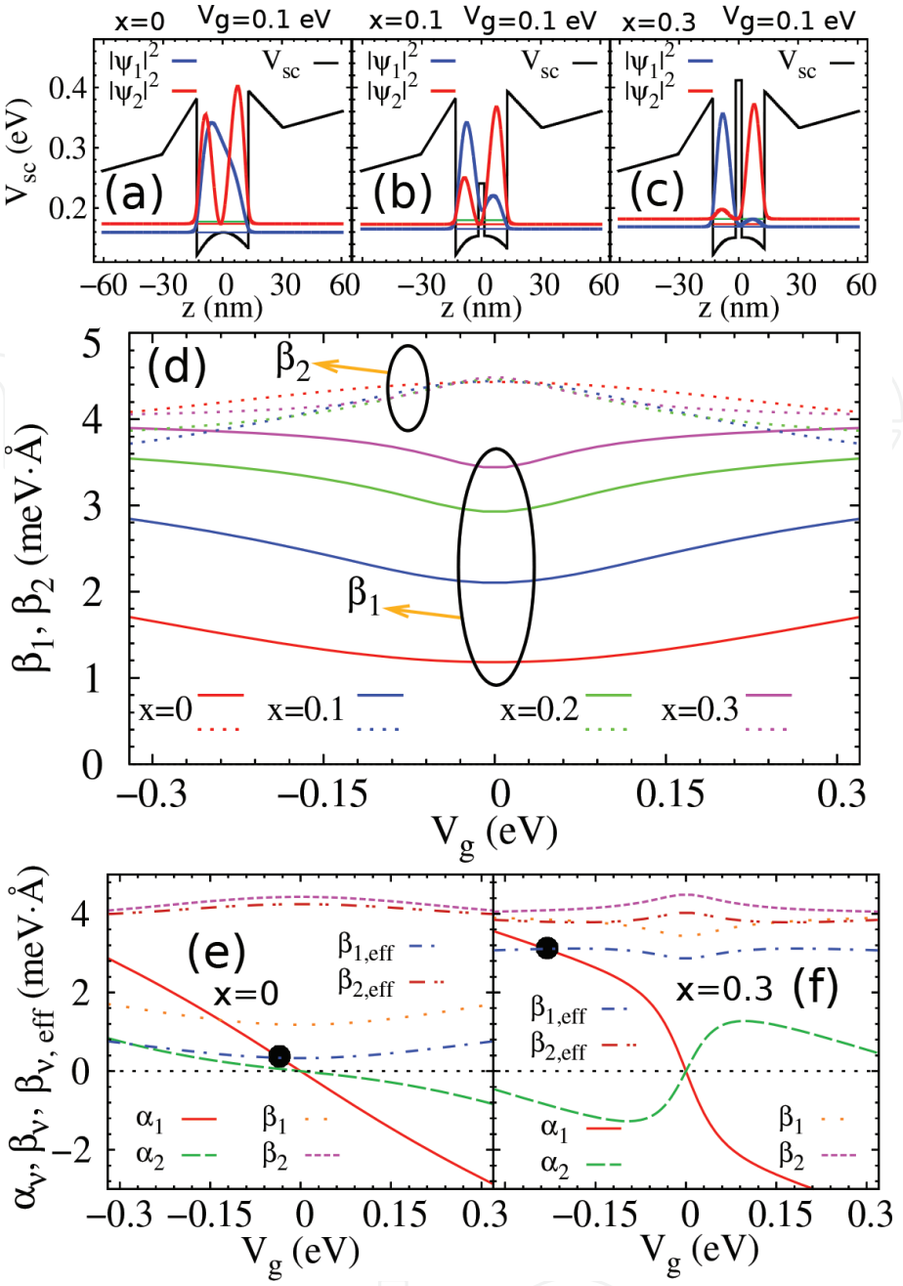

Figure 8.
(a)–(c) Self-consistent potential V_{sc} and wave function profiles ψ_ν for a GaAs/$Al_{0.3}Ga_{0.7}As$ well with $Al_xGa_{1-x}As$ as a central barrier, with $x = 0$ (a), 0.1 (b), and 0.3 (c). We consider $V_g = 0.1$ eV. The horizontal lines inside the well indicate the two-subband energy levels and the Fermi level. (d) Intrasubband Dresselhaus terms β_ν as a function of V_g, for several values of xs with $x = 0, 0.1, 0.2, 0.3$. (e) and (f) Gate dependence of SO strengths (α_ν, β_ν, $\beta_{\nu,eff}$) for $x = 0$ and $x = 0.3$, respectively. The black points indicate the PSH symmetry points (i.e., $\alpha_\nu = \pm\beta_{\nu,eff}$), from Wang et al. [40].

leading to a shrinking of the energy separation of the two subbands. Consequently, the strength of β_1 and β_2 becomes more close for a larger value of x.

Now, we determine the PSH symmetry points, where the Rashba α_ν and the renormalized linear Dresselhaus $\beta_{\nu,eff} = \beta_\nu - \beta_{\nu,3}$ are matched. The cubic Dresselhaus term $\beta_{\nu,3} = \gamma k_\nu^2/4 = \gamma\pi n_\nu/2$ depends on the electron occupations and therefore alters the condition of the PSH symmetry. **Figure 8**(**e**) and (**f**) show the gate dependence of α_ν, β_ν, and $\beta_{\nu,eff}$, for $x = 0$ and 0.3, respectively. Clearly, we see the distinction between β_ν and $\beta_{\nu,eff}$ because of the correction from $\beta_{\nu,3}$, in particular for the first subband, which has a higher electron occupation (see inset of **Figure 7**(**a**)). In the parameter range considered here, we only attain the PSH symmetry for the first subband ($\alpha_1 = \beta_{1,eff}$); see black point in **Figure 8**(**e**) and (**f**).

To attain the PSH symmetry for the second subband, one needs an even wider well [26], where β_2 is weaker so that α_2 and β_2 have the feasibility of matched strength by tuning V_g.

Besides altering the PSH symmetry condition involving SO terms of the first harmonic (sin / cos functions of θ), the cubic Dresselhaus $\beta_{3,\nu}$ also has the third harmonic (3θ) contribution; see Eq. (6). This leads to the decay of the PSH due to the D'yakonov-Perel' (DP) spin relaxation mechanism [41]. Specifically, the third harmonic Dresselhaus coupling-induced spin relaxation rate at the PSH symmetry point is written as $\Gamma_D^\nu = \gamma^2 k_\nu^6 \tau_P / 4\hbar^2$ [42], with τ_P the momentum relaxation time. For GaAs wells, with $\gamma \sim 11.0$ eV°A3, $k_\nu \sim 0.2$ nm^{-1}, and $\tau_P \sim 1.0$ ps [13, 31], we find $\Gamma_D^\nu \sim 0.07$ ns^{-1}.

In **Figure 9**(**a**) and (**b**), we show the gate dependence of the intersubband Rashba η and Dresselhaus Γ couplings, which depend on the overlap of the wave functions of the two subbands; see Eqs. (8) and (9). For the intersubband Rashba coupling η, we find that it remains essentially constant at $x = 0$, since ψ_1 and ψ_2 are well overlapped even at asymmetric configurations; see **Figure 8**(**a**) with $V_g = 0.1$ eV. However, when x is nonzero, electrons of the two subbands have the tendency of localizing on opposite sides of the well at asymmetric configurations (**Figure 8**(**b**) and (**c**)), namely, ψ_1 and ψ_2 tend to be separated. Therefore, η exhibits the strongest at the symmetric configuration of the system (i.e., $V_g = 0$). Note that at the symmetric configuration, ψ_1 and ψ_2 are perfectly overlapped. Furthermore, the separation of ψ_1 and ψ_2 is more distinct for a larger x (same V_g), cf. **Figure 8**(**b**) and (**c**),

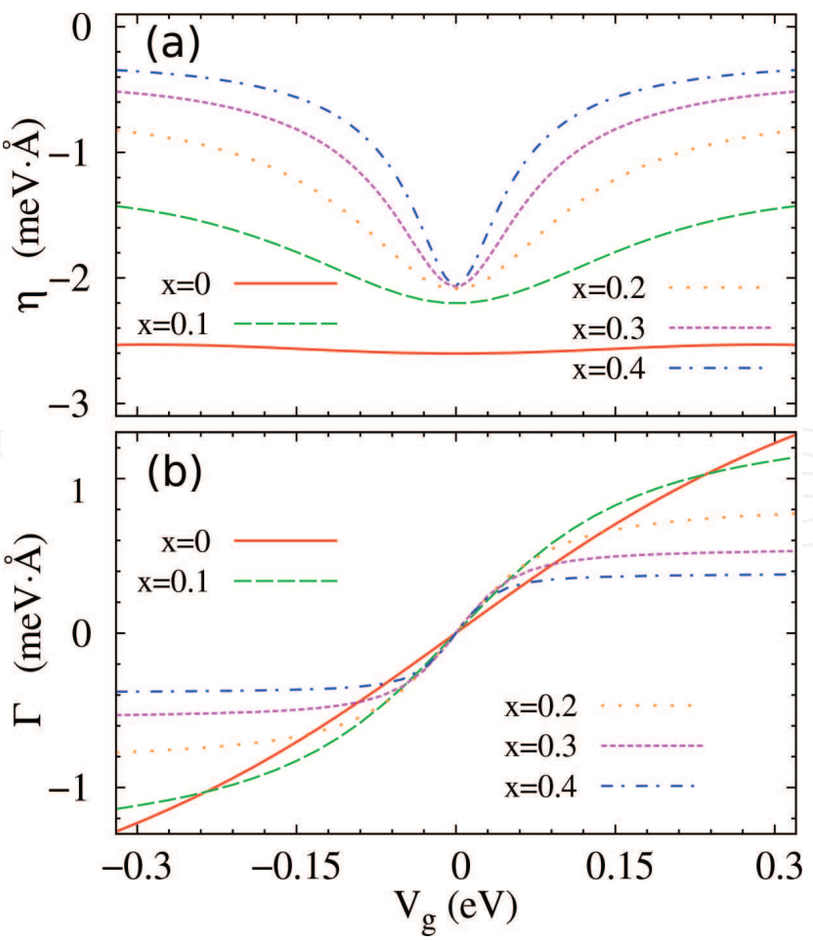

Figure 9.
Intersubband Rashba η (a) and Dresselhaus Γ (b) couplings as a function of V_g *in GaAs/*$Al_{0.3}Ga_{0.7}As$ *wells, for several Al contents x of the central barrier* $Al_xGa_{1-x}As$ *with* $x = 0, 0.1, 0.2, 0.3, 0.4$, *from Wang et al. [40].*

which renders η more sensitively dependent on V_g near $V_g = 0$. As for the intersubband Dresselhaus term $\Gamma = \langle 1|k_z^2|2\rangle$, on the one hand, it depends on the overlap of ψ_1 and ψ_2 and accordingly strongly depends on V_g near $V_g = 0$, similar to η. On the other hand, as opposed to η, the term Γ vanishes at $V_g = 0$ and further changes sign across the symmetric configuration, similar to the intrasubband Rashba terms α_ν.

Finally, we consider the case of our system having two additional barriers, namely, a triple well. As compared to the double well case, the wave functions of the two subbands ψ_1 and ψ_2 are more overlapped in a triple well under the same external conditions (e.g., same V_g), cf. **Figure 10**(**a**) and (**b**), due to the electron distribution in the middle of three wells. As a consequence, the relatively smooth change of SO terms even near the symmetric configuration follows when V_g varies, as shown in **Figure 10**(**c**). Moreover, we find that the Dresselhaus term β_ν is stronger than that in our double well, cf. **Figures 8**(**d**) and **10**(**c**). Note that the basic feature of the electrical control of the SO interaction in our triple well is similar to that in the double well, for the parameter range studied, under which the two-subband electron occupancy occurs.

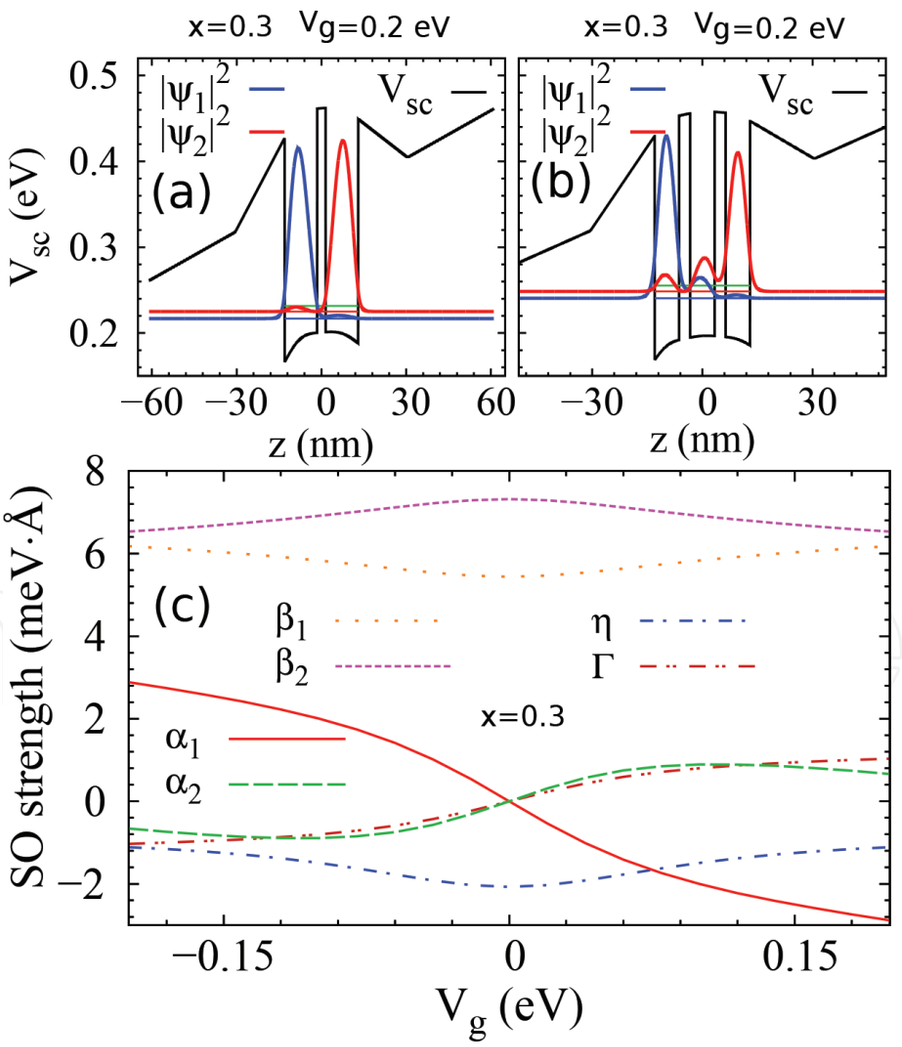

Figure 10.
Confining potential and the two-band wave function for a GaAs/$Al_{0.3}Ga_{0.7}As$ double well (a) and triple well (b) with embedded barrier $Al_xGa_{1-x}As$ of $x = 0.3$, at $V_g = 0.2$ eV. The horizontal lines inside the well indicate the two-subband energy levels and the Fermi level (c). gate control of intrasubband Rashba (α_ν) and Dresselhaus (β_ν) and Intersubband Rashba (η) and Dresselhaus (Γ) for the GaAs/$Al_{0.3}Ga_{0.7}As$ triple well with the embedded barrier $Al_xGa_{1-x}As$ of $x = 0.3$, from Wang et al. [40].

5. Conclusion

In this chapter, firstly, we consider two distinct regimes of the control of the SO interaction in conventional semiconductor quantum wells. Specifically, we have performed a detailed self-consistent calculation on realistic GaAs wells with gate-altered electron occupations from two subbands to one subband, thus determining how the SO coupling (both the magnitude and sign) changes as a function of the gate voltage V_g. We have considered a set of wells of the width w in a wide range and found two distinct regimes. In the first regime, the behavior of the SO interaction is usual, e.g., a linear gate control of the Rashba terms. In contrast, in the second regime, there are emerging new features that one has to pay attention to when controlling SO couplings, e.g., the relative signs (same or opposite) of α_1 and α_2 can be controlled by the gate, α_2 can attain zero in certain asymmetric configurations, and α_2 remains essentially constant within a particular gate voltage range. In addition, we have determined the persistent-spin-helix symmetry points of the two subbands and found that the condition $\alpha_2 = -\beta_{2,\,eff}$ always holds over a broad range of V_gs, thus possibly facilitating the locking of the symmetry point for the second subband in practice. Some of these features in the second regime can in principle be observed in proper double-well structures [24], as wide wells behave like "effective" double wells owing to the electron Hartree potential-induced central barrier. Moreover, the "symmetric configuration" mentioned throughout this work only refers to regions near the well (i.e., not far into the barriers). We cannot make our wells universally/fully symmetric by only tuning the gate voltage, due to the one-side doping in our system. This *partial* symmetric configuration is enough to render the intrasubband Rashba couplings to zero, since the envelope wave functions decay very quickly into the barriers. Our results should be timely and important for experiments controlling/tailoring the SO coupling *universally*, particularly for the *unusual* electrical control of the SO coupling in the second regime.

Secondly, we have investigated the full scenario of the electrical control of the SO interaction in a realistic GaAs/$Al_{0.3}Ga_{0.7}As$ well with one or two additional $Al_xGa_{1-x}As$ barriers embedded, in the course of the transition of our system from single to double and triple wells. We constantly consider the two-subband electron occupancy for all values of gate voltage V_g studied here. As the Al content of the embedded barrier(s) x varies, we find distinct scenarios of the electrical control of SO terms, e.g., linear or nonmonotonic dependence of α_2 on V_g, same or opposite signs between α_1 and α_2, and inert or abrupt change of η with V_g near the symmetric configuration. In addition, we find that the gate dependence of SO terms is more smooth and β_ν is more stronger in our triple well, compared to the double well case. Moreover, we observe that the basic scenario of the electrical control of the SO interaction in our triple and double wells is similar, in the parameter range studied here. These results are expected to be important for a broad control of the SO interaction in semiconductor nanostructures.

As a final remark, in the case of three-subband electron occupancy which is not considered here, the electrical control of SO couplings is possibly distinct between double and triple wells because of a higher third subband occupation. More work is needed to investigate this interesting possibility (higher electron density).

Acknowledgements

This work was supported by the National Natural Science Foundation of China (Grant No. 11874236), FAPESP, and Capes.

Author details

Jiyong Fu[1*], Wei Wang[2] and Minghua Zhang[2]

1 Department of Physics, Qufu Normal University, Qufu, Shandong, China

2 Department of Physics, Jining University, Qufu, Shandong, China

*Address all correspondence to: jiyongfu78@gmail.com

IntechOpen

References

[1] Awschalom D et al. Semiconductor Spintronics and Quantum Computation. New York: Springer; 2002

[2] Žutić I et al. Spintronics: Fundamentals and applications. Reviews of Modern Physics. 2004;**76**:32

[3] Datta S, Das B. Electronic analog of the electro-optic modulator. Applied Physics Letters. 1990;**56**:665

[4] Winkler R. Spin-Orbit Coupling Effects in Two-Dimensional Electron and Hole Systems. Berlin and New York: Springer; 2003

[5] Schliemann J et al. Nonballistic spin-field-effect transistor. Physical Review Letters. 2003;**90**:146801

[6] Bernevig BA et al. Exact SU(2) symmetry and persistent spin helix in a spin-orbit coupled system. Physical Review Letters. 2006;**97**:236601

[7] Koralek JD et al. Emergence of the persistent spin helix in semiconductor quantum wells. Nature. 2009;**458**:610

[8] Walser MP et al. Direct mapping of the formation of a persistent spin helix. Nature Physics. 2012;**8**:757

[9] Bernevig BA et al. Quantum spin hall effect and topological phase transition. Science. 2006;**314**:1757

[10] Lutchyn RM et al. Majorana fermions and a topological phase transition in semiconductor-superconductor heterostructures. Physical Review Letters. 2010;**105**: 077001

[11] Oreg Y et al. Helical liquids and majorana bound states in quantum wires. Physical Review Letters. 2010; **105**:177002

[12] Dresselhaus G. Spin-orbit coupling effects in zinc blende structure. Physics Review. 1955;**100**:580

[13] Dettwiler F et al. Stretchable persistent spin helices in GaAs quantum wells. Physical Review X. 2017;**7**:031010

[14] Bychkov YA, Rashba EI. Properties of a 2D electron gas with lifted spectral degeneracy. JETP Letters. 1984;**39**:78

[15] Engels G et al. Exact exchange plane-wave-pseudopotential calculations for slabs: Extending the width of the vacuum. Physical Review B. 1997;**55**:R1958

[16] Nitta J et al. Gate control of spin-orbit interaction in an inverted In0.53Ga0.47As/In0.52Al0.48As heterostructure. Physical Review Letters. 1997;**78**:1335

[17] Sasaki A et al. Direct determination of spin–orbit interaction coefficients and realization of the persistent spin helix symmetry. Nature Nanotechnology. 2014;**90**:703

[18] Hernandez FGG et al. Observation of the intrinsic spin hall effect in a two-dimensional electron gas. Physical Review B. 2013;**88**:161305(R)

[19] Bentmann H et al. Direct observation of interband spin-orbit coupling in a two-dimensional electron system. Physical Review Letters. 2012;**108**:196801

[20] Hu CM et al. Zero-field spin splitting in an inverted In0.53Ga0.47As/ In0.52Al0.48As heterostructure: Band nonparabolicity influence and the subband dependence. Physical Review B. 1999;**60**:7736

[21] Kavokin KV et al. Spin-orbit terms in multi-subband electron systems: A bridge between bulk and

two-dimensional Hamiltonians. Semiconductors. 2008;**42**:989

[22] de Andrada e Silva EA et al. Spin-orbit splitting of electronic states in semiconductor asymmetric quantum wells. Physical Review B. 1997;**55**:16293

[23] Bernardes E et al. Spin-orbit interaction in symmetric wells with two subbands. Physical Review Letters. 2007;**90**:076603

[24] Calsaverini RS et al. Intersubband-induced spin-orbit interaction in quantum wells. Physical Review B. 2008;**78**:155313

[25] Fu JY et al. Persistent skyrmion lattice of noninteracting electrons with spin-orbit coupling. Physical Review Letters. 2016;**117**:226401

[26] Fu JY, Carlos Egues J. Spin-orbit interaction in GaAs wells: From one to two subbands. Physical Review B. 2015; **91**:075408

[27] Goni AR, Haboeck U, Thomsen C, Eberl K, Reboredo FA, Proetto CR, et al. Exchange instability of the two-dimensional electron gas in semiconductor quantum wells. Physical Review B. 2002;**65**:121313(R)

[28] Rigamonti S, Proetto CR. Signatures of discontinuity in the exchange-correlation energy functional derived from the subband electronic structure of semiconductor quantum wells. Physical Review Letters. 2007;**98**:066806

[29] Vurgaftman I et al. Band parameters for III-V compound semiconductors and their alloys. Journal of Applied Physics. 2001;**89**:5815

[30] Yi W et al. Bandgap and band offsets determination of semiconductor heterostructures using three-terminal ballistic carrier spectroscopy. Applied Physics Letters. 2009;**95**:112102

[31] Walser MP et al. Dependence of the Dresselhaus spin-orbit interaction on the quantum well width. Physical Review B. 2012;**86**:195309

[32] Wang W et al. Two distinct regimes for the electrical control of the spin–orbit interaction in GaAs wells. Journal of Magnetism and Magnetic Materials. 2016;**411**:84

[33] Kunihashi Y et al. Proposal of spin complementary field effect transistor. Applied Physics Letters. 2012;**100**: 113502

[34] Sheng XL et al. Topological insulator to Dirac semimetal transition driven by sign change of spin-orbit coupling in thallium nitride. Physical Review B. 2014;**90**:245308

[35] Fletcher R et al. Two-band electron transport in a double quantum well. Physical Review B. 2005;**71**:155310

[36] Glazov MM et al. Two-dimensional electron gas with spin-orbit coupling disorde. Physica E. 2010;**42**:2157

[37] Morgenstern M et al. Scanning tunneling microscopy of two-dimensional semiconductors: Spin properties and disorder. Physica E. 2012; **44**:1795

[38] Glazov MM, Sherman EY. Nonexponential spin relaxation in magnetic fields in quantum wells with random spin-orbit coupling. Physical Review B. 2005;**71**:241312(R)

[39] Sherman EY. Random spin-orbit coupling and spin relaxation in symmetric quantum wells. Applied Physics Letters. 2003;**82**:209

[40] Wang W, Fu JY. Electrical control of the spin-orbit coupling in GaAs from single to double and triple wells. Superlattices and Microstructures. 2015; **88**:43

[41] D'yakonov MI, Perel' VI. Spin orientation of electrons associated with the interband absorption of light in semiconductors. Soviet Physics–JETP. 1971;**33**:1053

[42] Meier F, Zakharchenya BP. Optical Orientation. Amsterdam: North-Holland; 1984